

Electrical control of orbital and vibrational interlayer coupling in bi- and trilayer 2H-MoS<sub>2</sub>J. Klein<sup>1,2,\*</sup>, J. Wierzbowski,<sup>1</sup> P. Soubelet<sup>1</sup>, T. Brumme<sup>3,4</sup>, L. Maschio<sup>5</sup>, A. Kuc<sup>6,7</sup>, K. Müller<sup>8</sup>, A. V. Stier<sup>1,†</sup> and J. J. Finley<sup>1,‡</sup><sup>1</sup>Walter Schottky Institut and Physik Department, Technische Universität München, Am Coulombwall 4, 85748 Garching, Germany<sup>2</sup>Department of Materials Science and Engineering, Massachusetts Institute of Technology, Cambridge, Massachusetts 02139, USA<sup>3</sup>Wilhelm-Ostwald-Institute for Physical and Theoretical Chemistry, Leipzig University, Liné Str. 2, 04103 Leipzig, Germany<sup>4</sup>Faculty for Chemistry and Food Chemistry, TU Dresden, Bergstrasse 66c, 01069 Dresden, Germany<sup>5</sup>Dipartimento di Chimica and Centre of Excellence NIS (Nanostructured Interfaces and Surfaces), Università di Torino, via P. Giuria 5, I-10125 Turin, Italy<sup>6</sup>Helmholtz-Zentrum Dresden-Rossendorf, Abteilung Ressourcenökologie, Forschungsstelle Leipzig, Permoserstr. 15, 04318 Leipzig, Germany<sup>7</sup>Department of Physics and Earth Sciences, Jacobs University Bremen, Campus Ring 1, 28759 Bremen, Germany<sup>8</sup>Walter Schottky Institut and Department of Electrical and Computer Engineering, Technische Universität München, Am Coulombwall 4, 85748 Garching, Germany

(Received 24 June 2021; revised 19 December 2021; accepted 7 January 2022; published 7 February 2022)

Manipulating electronic *interlayer* coupling in layered van der Waals (vdW) materials is essential for designing optoelectronic devices. Here, we control vibrational and electronic interlayer coupling in bi- and trilayer 2H-MoS<sub>2</sub> using large external electric fields in a microcapacitor device. The electric field lifts Raman selection rules and activates phonon modes in excellent agreement with *ab initio* calculations. Through polarization-resolved photoluminescence spectroscopy in the same device, we observe a strongly tunable valley dichroism with maximum circular polarization degree of  $\sim 60\%$  in bilayer and  $\sim 35\%$  in trilayer MoS<sub>2</sub> that is fully consistent with a rate equation model which includes input from electronic band structure calculations. We identify the highly delocalized electron wave function between the layers close to the high-symmetry  $Q$  points as the origin of the tunable circular dichroism. Our results demonstrate the possibility of electric-field-tunable interlayer coupling for controlling emergent spin-valley physics and hybridization-driven effects in vdW materials and their heterostructures.

DOI: [10.1103/PhysRevMaterials.6.024002](https://doi.org/10.1103/PhysRevMaterials.6.024002)

## I. INTRODUCTION

Breaking of crystal symmetries has profound effects on the electrical [1–3] and optical properties [4–7] of van der Waals (vdW) bonded materials and their heterostructures [8]. A prime example is bilayer graphene, where an applied electric field breaks crystal inversion symmetry that opens up a band gap [1] and induces, e.g., topological valley currents [2,3]. Monolayer transition-metal dichalcogenides (TMDCs), like MoS<sub>2</sub>, exhibit valley dichroism, due to their inherently broken inversion symmetry, where  $K$  valleys are related to one another via time-reversal symmetry, as governed by the Kramers degeneracy [9–14]. The 2H stacking results in alternating point groups with odd layer numbers manifesting in broken spatial inversion symmetry that is restored in either even-layer crystals or evenly layered crystals. Several intriguing experimental observations, including electrical tuning of valley-magnetic moment [4], spin-layer locking [5], and finite valley Hall effect [6], have been reported in bilayer TMDCs and ascribed to the control of Berry curvature, due to inversion symmetry breaking by an external electric field [15].

In such multilayered systems, *interlayer* hopping of electrons or holes plays a crucial role for the formation of interlayer excitonic complexes [16–24]. The redistribution of charge carriers is realized by an ultrafast charge transfer between the layers [18,25]. Here, the application of an external electric field can control the layer hybridization [21,26–28] and tune hopping rates between individual layers to control photophysical properties. Therefore, realizing field-controlled multilayer devices made from TMDCs may offer novel device designs to control, e.g., spin-valley polarization for prospective optoelectronic devices.

In this paper, we electrically control the *interlayer* hybridization in bi- and trilayer MoS<sub>2</sub>. From our measurements, we observe electric-field-activated Raman modes, where the relative mode intensity is a qualitative fingerprint for the degree of interlayer (de)coupling in the context of a change in interlayer hybridization. The observed activated phonon modes are in excellent agreement with *ab initio* density functional theory (DFT) calculated phonon spectra that include external electric fields. The phonon mode activation correlates with a highly tunable degree of circular polarization  $\eta$  of the  $A$ -exciton emission in inversion-symmetric bilayer MoS<sub>2</sub>, with values varying with the electric field from  $\eta \sim 0.2$  up to 0.6, limited only by the maximally explored gate voltage. Strikingly, the trilayer sample, which is intrinsically inversion symmetry broken, also reveals a tunable  $\eta \sim 0.2$ -0.36, unlike

\*jpklein@mit.edu

†andreas.stier@wsi.tum.de

‡finley@wsi.tum.de

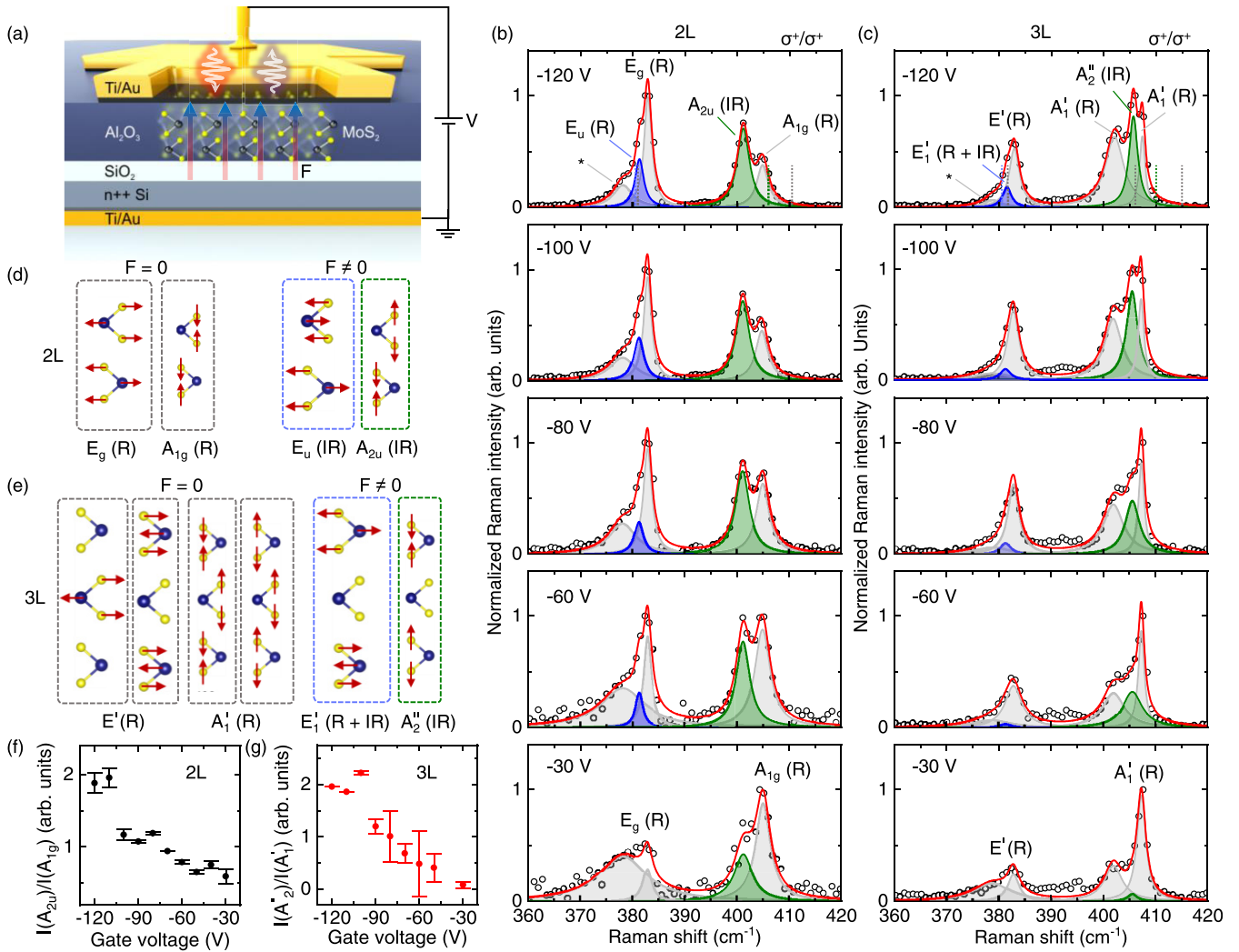


FIG. 1. (a) Schematic illustration of the microcapacitor device. Few-layer MoS<sub>2</sub> is electrically isolated due to encapsulation between SiO<sub>2</sub> and Al<sub>2</sub>O<sub>3</sub>. The 5-nm-thick Ti top gate allows optical access while out-of-plane electric fields are applied. (b) Voltage-dependent low-temperature (10 K) Raman spectra for bilayer MoS<sub>2</sub>. Breaking of crystal symmetry from the external electric field activates the intensity of the Raman modes  $E_u$  (R) (blue) and  $A_{2u}$  (IR) (green). \* denotes a voltage-independent background accounted for with a Lorentzian peak. (c) Voltage-dependent Raman spectra for trilayer MoS<sub>2</sub>. The electric field activates the intensity of the Raman modes  $E'_u$  (R + IR) (blue) and  $A'_2$  (IR) (green). Dashed lines highlight corresponding calculated phonon frequencies. Atomic displacement of Raman modes in (d) bilayer and (e) trilayer MoS<sub>2</sub> with and without electric field. Dashed lines highlight corresponding calculated phonon frequencies. (f) Ratio of the Raman intensities  $A_{2u}$  and  $A_{1g}$  indicate a phenomenological measure of vibrational symmetry breaking in the bilayer. (g) Ratio of the Raman intensities of  $A'_2$  and  $A'_1$  in the trilayer.

the monolayer MoS<sub>2</sub>, where  $\eta$  is field independent. We interpret our observations in terms of the electric-field-dependent conduction and valence band edges at the  $K$  and  $K'$  and  $Q$  and  $Q'$  points. The external electric field changes the interlayer hybridization; most importantly for our experiments, the electron wave function distribution between the layers at the  $Q$  and  $Q'$  points results in an electric-field-dependent population of optically excited electrons and holes in the layers at the  $K$  and  $K'$  points. We support our observations with a rate-equation model that takes into account the *ab initio* calculated electronic band structure. Our results show that the  $Q$  points significantly influence electron hopping in 2H-multilayered TMDC crystals, and that the concept of symmetry alone is insufficient to explain optical dichroism in few-layer MoS<sub>2</sub> but that *interlayer* coupling and, in particular, the hopping

of electrons strongly influence the redistribution of optically excited carriers in the multilayer sample. Our results further demonstrate the potential to control emergent spin- and valleytronic devices based on two-dimensional (2D) atomically thin crystals with electric fields.

## II. RESULTS AND DISCUSSION

### A. Microcapacitor device

The investigated device consists of mono-, bi-, and trilayer 2H-MoS<sub>2</sub> embedded in a micro-capacitor structure. [7,29] The layers are electrically isolated from the contacts, as depicted schematically in Fig. 1(a). A 5-nm-thick semi-transparent titanium top gate facilitates optical access to the crystals, while applying a gate voltage in the range of  $\pm 120$  V

TABLE I. Experimental and theoretical frequencies of phonon modes of bi- and trilayer MoS<sub>2</sub> with an external electric field.

	Mode	$\omega_{\text{expt}}$ (cm <sup>-1</sup> )	$\omega_{\text{theor}}$ (cm <sup>-1</sup> )
2L	$E_u(R)$	381.24 ± 0.40	381.5
	$E_g(R)$	382.81 ± 0.05	381.7
	$A_{2u}(IR)$	401.17 ± 0.08	407
	$A_{1g}(R)$	404.81 ± 0.14	412
3L	$E'(R + IR)$	381.5 ± 0.83	380.9
	$E'(R)$	382.91 ± 0.15	381.4
	$A'_1(R)$	402.05 ± 0.11	406
	$A'_2(IR)$	405.67 ± 0.05	410
	$A'_1(R)$	407.39 ± 0.05	415

results in electric fields on the order of MV cm<sup>-1</sup>. Raman and photoluminescence (PL) data are acquired keeping the device at a lattice temperature of 10 K and optically exciting at an energy of 1.96 eV.

### B. Activation of Raman modes by crystal symmetry breaking

We now explore the phonon properties in this microcapacitor device. The lattice vibrational modes in 2D materials encode rich information of crystal symmetries that can be directly derived from group theory [30,31]. The irreducible representations of bilayer and trilayer MoS<sub>2</sub> are  $\Gamma = 3(A_{1g} + E_g + A_{2u} + E_u)$  and  $\Gamma = 4(A'_1 + E'') + 5(A''_2 + E')$ , respectively. Here, the out-of-plane modes  $A_{1g}$  ( $A'_1$ ) are Raman active (R) while the  $A_{2u}$  ( $A''_2$ ) are infrared active (IR). The in-plane mode  $E_g$  in the bilayer is Raman active while the  $E_u$  mode is infrared active. In the trilayer the  $E'$  mode is Raman active while the  $E'_1$  mode is both Raman and infrared active [32]. Both  $E_g$  ( $E'$ ) and  $A_{1g}$  ( $A'_1$ ) modes are active in our backscattering geometry. In order to study the effect of perturbing the crystal symmetry using an out-of-plane electric field, we now tune the gate voltage and study phonon modes.

Gate-voltage-dependent data for bi- and trilayer MoS<sub>2</sub> are presented in Figs. 1(b) and 1(c). For maximally broken inversion symmetry in the bilayer and also in the trilayer ( $V = -120$  V in our device) additional phonon modes (colored blue and green) appear in the spectrum [see Figs. 1(b) and 1(c)]. Their intensity monotonically decreases with decreasing gate voltage.

To understand the origin of the phonon modes for an applied external electric field, we perform *ab initio* DFT calculations of phonon spectra for mono-, bi-, and trilayer MoS<sub>2</sub> with and without electric field (see full phonon dispersion in the Supplemental Material [33]). Our calculations indeed suggest additional phonon modes,  $E_u$  (IR) ( $E'_1$  (R + IR)) and  $A_{2u}$  (IR) ( $A''_2$  (IR)) in the bilayer (trilayer) with corresponding displacements shown in Figs. 1(d) and 1(e). Such modes are present in our calculations in both zero and finite electric fields but have zero Raman intensity for no applied electric field. The application of an electric field enhances the Raman intensity of the additional modes due to the lifting of Raman selection rules. The experimental and theoretical values of phonon modes of bi- and trilayer MoS<sub>2</sub> are summarized in Table I and further highlighted in the Raman spectra in Figs. 1(b) and 1(c). The calculated absolute phonon mode

energies and their frequency differences are in excellent agreement with our experimental spectra. To quantify the extent to which symmetry is broken by the external electric field, we plot the ratio of phonon mode intensities between the  $A_{2u}$  and  $A_{1g}$  modes for the bilayer MoS<sub>2</sub> and  $A''_2$  and  $A'_1$  modes for the trilayer MoS<sub>2</sub> [see Figs. 1(f) and 1(g)]. As expected, the highest ratio (degree of symmetry breaking) is observed for the highest gate voltage  $V = -120$  V (electric field) while the ratio vanishes for decreasing gate voltages  $V = -30$  V. The offset from  $V = 0$  V originates from the asymmetric dielectric environment and built-in electric field of the device as discussed in detail in Refs. [7,29]. Note that we focus our discussion on negative gate voltages since the total Raman intensity strongly diminishes at positive voltages due to carrier doping effects in the asymmetric device structure [34], which originate from charge transfer for this field polarity from the Al<sub>2</sub>O<sub>3</sub> interface into the MoS<sub>2</sub> [7,29]. This is further reflected by the nonshifting out-of-plane Raman modes for negative voltages (see the Supplemental Material [33]), a clear indication that the electric field is dominant for such voltages [35]. We can conclude that the appearance of new Raman modes for an applied electric field is a direct fingerprint for the change in Raman selection rules in our tunable microcapacitor device. The observation of such modes was reported in WS<sub>2</sub> as a consequence of resonant excitation on the *A*-exciton transition [36,37] that can lift the Raman selection rules, similar to our experimental setup. The observation of such modes in our experiment is the combination of the finite electric field that results in a finite Raman intensity of the modes in our microcapacitor device in combination with the resonant laser excitation of the *A* exciton.

### C. Electrical control of interlayer hybridization

We now directly correlate the observed crystal symmetry breaking from our Raman measurements with circularly polarized  $\mu$ -PL of 1L, 2L, and 3L MoS<sub>2</sub>. All measurements are performed with quasis resonant excitation of the *A* exciton using a continuous wave HeNe laser emitting at 1.96 eV and the samples at a lattice temperature of  $T = 10$  K. Polarization-resolved PL spectra are recorded with  $\sigma^+$ -polarized (and  $\sigma^-$ -polarized) excitation and the emitted PL is analyzed with  $\sigma^+$  and  $\sigma^-$  discrimination. Both sets of data are equivalent since the *K* and *K'* valleys are equivalent. The resulting PL spectra are denoted  $I^\pm(E)$ , where the superscript denotes the helicity of the polarization discrimination in the detection channel and  $E$  is the energy of the emitted photons.

Typical gate-voltage-dependent degree of valley polarization  $\eta$  and the corresponding spectra recorded at  $V = -60$  V and  $V = -120$  V are shown in Fig. 2. We observe the direct gap *A*-exciton transition in all spectra at  $\sim 1.875$  eV. The degree of circular polarization is derived from the PL  $I^+$  and  $I^-$  spectra that is defined by  $\eta(E) = (I^+(E) - I^-(E))/(I^+(E) + I^-(E))$  and plotted in addition to the PL spectra in Fig. 2(b). The PL in monolayer MoS<sub>2</sub> is strongly circularly polarized with  $\eta \sim 80\%$ . In general,  $\eta$  is a measure for the optically excited steady-state carrier populations in the *K* and *K'* valleys [schematically shown in Fig. 2(a)] reflecting the interplay between the *interband* optical selection rules, as well as *intra*- and *intervalley* relaxation dynamics that occur due to

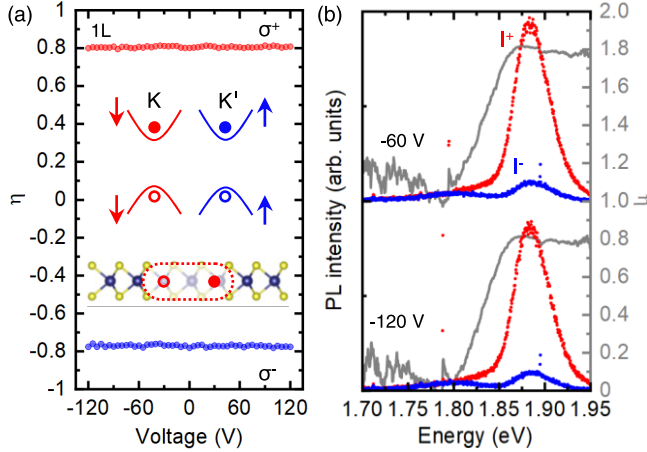


FIG. 2. (a) Gate-voltage-independent degree of circular polarization  $\eta$  for monolayer MoS<sub>2</sub> with  $\sigma^+$  (red) and  $\sigma^-$  (blue) excitation. Inset: Valley and spin *interband* optical selection rules at  $K$  and  $K'$  and *intralayer* exciton. (b) Low-temperature circularly polarized  $\mu$ -PL spectra for 1L taken at  $-60$  and  $-120$  V. Blue (red) spectra are obtained for  $\sigma^+$  excitation and  $\sigma^+$  ( $\sigma^-$ ) detection. The degree of valley polarization is plotted in grey.

thermalization, and radiative recombination lifetimes [38,39]. For the monolayer, we observe a field-independent  $\eta$ , which is a direct consequence of the inherently broken inversion symmetry and field-independent *intervalley* scattering [4]. As evident from the data,  $\eta$  for monolayer MoS<sub>2</sub> is constant throughout the whole range of applied gate voltages with a high value of  $|\eta_{\text{IL}}^{\text{max}}| = 0.8$  in good agreement with previous reports [4,11,12,40].

Unlike the monolayer, the inversion-symmetric bilayer shows a strongly tunable  $\eta$  [see Fig. 3(a)]. Here, we observe the lowest  $\eta = 0.2$  for  $V = -60$  V where crystal symmetry is maximally restored in our asymmetric device in very good agreement with the absence of field-activated Raman modes [see Fig. 1(b)]. In contrast, for  $V = -120$  V, symmetry is maximally broken in our device for which we also observe the field-activated Raman modes with highest intensity. This observation clearly reflects the lifted crystal inversion symmetry, and therefore the change in the electronic *interlayer* coupling directly affecting the degree of valley polarization in the bilayer.

In general, the experimental degree of valley polarization in bilayer TMDCs varies widely in the literature. Near-unity values are experimentally observed for WSe<sub>2</sub> and WS<sub>2</sub>, very likely due to the dark band alignment in both the single-particle picture and the exciton picture resulting in locking of the spin and layer pseudospin in individual layers [5,41]. In contrast, very low values for MoS<sub>2</sub> ( $\sim 20\%$ ) [4,11,24,42] and MoSe<sub>2</sub> ( $\sim 10\%$ ) [43] are observed. One explanation is the bright single-particle band structure of MoS<sub>2</sub> and MoSe<sub>2</sub>, while the case for MoS<sub>2</sub> is even more intricate due to a dark conduction band alignment in the exciton picture [44–46].

External electric fields can change layer hybridization and break symmetries that can alter the valley polarization in bilayer TMDCs [4–6]. Control of valley polarization has

been tentatively attributed to breaking of global space-group inversion symmetry, but recent theoretical work suggests that the circular polarization originates from inversion symmetry breaking of atomic site point groups and/or local sectors [47–49].

Considering the weak *interlayer* coupling in TMDCs, the relaxation dynamics are expected to significantly depend on the hybridization of sulfur  $p$  orbitals between proximal layers in MoS<sub>2</sub>. While the conduction bands at  $K$  and  $K'$  show only a weak admixture of the sulfur  $p$  orbitals since they are mainly comprised of Mo  $d$  orbitals, the  $Q$  points have a predominant contribution from the  $p$  orbitals [50]. The relevant high-symmetry points in momentum space of the coupled bilayer system are schematically depicted in Fig. 3(b). The  $Q$  points strongly connect the top and bottom layers, which is also directly apparent from the strong delocalization of our DFT-computed wave function at the  $Q$  point [see Fig. 3(c)]. Note that holes in multilayer MoS<sub>2</sub> also show a delocalization between  $K$  points [21,51–55]; however, this delocalization is much weaker as compared to the strong delocalization of electrons in the CB at  $Q$  (see Supplemental Material [33] for additional wave-function calculations at the  $K$  point).

Our experiments show that when the excitation is circularly polarized, for instance  $\sigma^+$ , and resonant with the  $A$  exciton, a fraction  $s$  of light is emitted with opposite helicity, even when the crystal symmetry is maximally restored ( $V \sim -60$  V). This recombination channel implies an *intervalley* scattering of carriers that is independent of the applied gate voltage and should be also present in multilayered structures. For this reason, the amount of light emitted with opposite helicity has been considered as constant; i.e.,  $s$  is constant and equal to the  $\sigma^-$  emission when the excitation is  $\sigma^+$  polarized and vice versa. The variation of  $\eta$  as a function of the gate voltage is an effect that can only be observed in multilayered systems and is the result of an interplay between the realignment of the hybridized bands and transfer of photoexcited carriers through different layers.

To explain the degree of polarization in the PL emission of multilayered systems, we consider only the  $\sigma^+$  excitation. For no applied voltage (electric field), the energies of  $Q$  and  $K$  valleys in both layers are energetically degenerate [see Fig. 3(d)], resulting in minimal charge transfer between the  $Q$  valleys between the individual layers. The application of a voltage (electric field) pushes the electrons from the top layer to the bottom layer [see Fig. 3(e)]. Since this model is symmetric, electric fields in the opposite directions and  $\sigma^-$  excitation are equivalent. The quiresonant excitation of a bilayer MoS<sub>2</sub> generates a steady-state electronic distribution in the CB with electrons residing in the  $Q$ ,  $Q'$ ,  $K$ , and  $K'$  valleys [Fig. 3(e)] [56–60]. As we consider only the scattering of electrons from  $Q$  to  $K$  valley and from  $Q'$  to  $K'$  valley, we analyze each case separately. Considering that we excited  $n_0$  electrons in each case, a fraction  $c$  of them reside in the  $K_1^\uparrow$  valley of the top layer, while  $(1 - c)n_0$  are in the  $Q$  valley, distributed through both layers [see dotted lines in Fig. 3(e)]. Without a gate voltage applied, the differential rate equations that describe the dynamics of these two levels are

$$\dot{n}_{K_1^\uparrow} = cn_0 - \frac{n_{K_1^\uparrow}}{\tau_K} - \frac{n_{K_1^\uparrow}}{T_K} \quad (1)$$

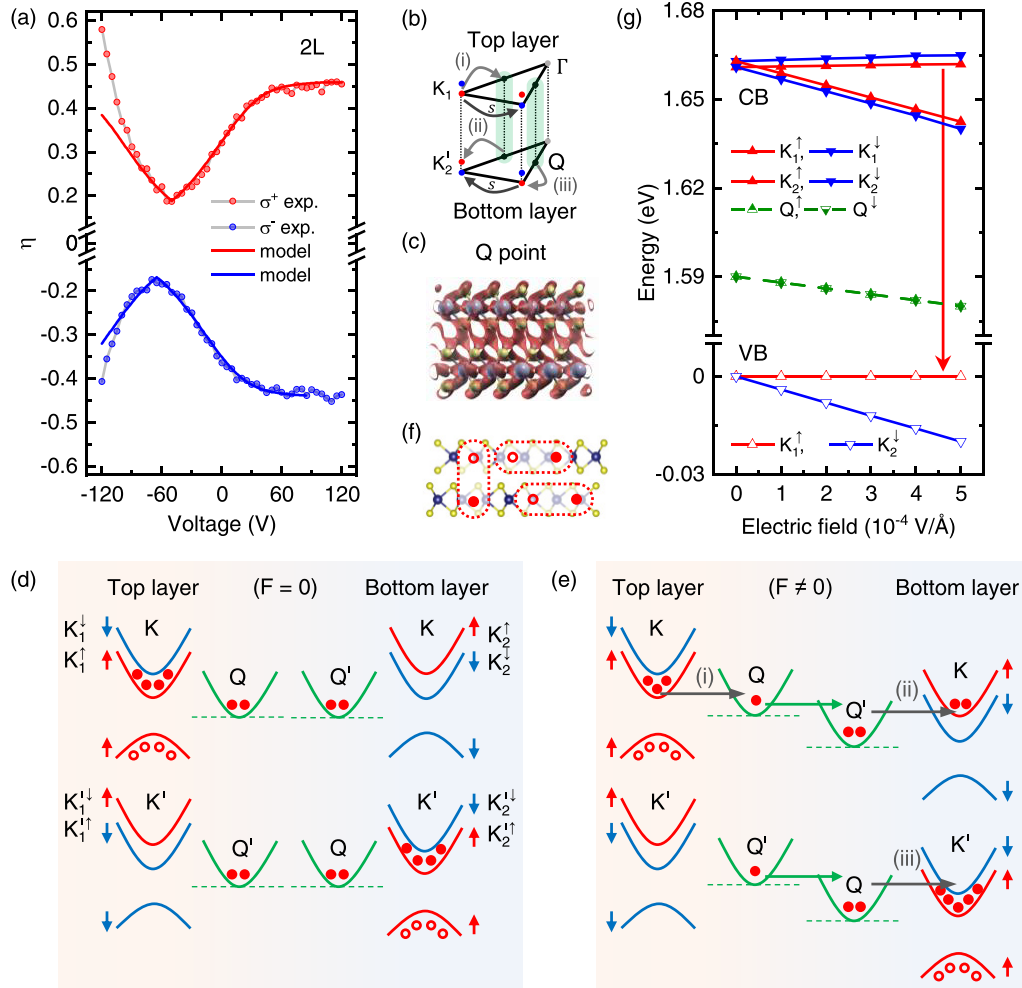


FIG. 3. (a) Tuning of orbital interlayer coupling in bilayer MoS<sub>2</sub>. Voltage-controlled degree of valley polarization for  $\sigma^+$  (red circles) and  $\sigma^-$  (blue circles) excitation. The solid lines are the calculated  $\eta$  from a rate-equation model. (b) First Brillouin zone and high-symmetry points of the bilayer MoS<sub>2</sub>. The scattering pathways (i)–(iii) of electrons are highlighted in addition to *intralayer* and *intervalley* scattering *s*. (c) *Ab initio* calculated wave function distribution at the *Q* point is strongly delocalized between top and bottom layers. (d, e) Schematics of the rate equation model and band alignment used for describing the tunable  $\eta$  in presence and absence of an external electric field. Valleys in red (blue) correspond to spin-up (spin-down) states. Grey arrows represent the electronic transitions promoted by the gate voltage and generates an electric field pointing from bottom to top layer. The green vertical arrows represent the polarization of the *Q* valleys that pushes the electrons from top layer to bottom layer. The conduction band (CB) electronic population is represented by red circles and holes are represented with open circles. (f) Schematic of intra- and *interlayer* excitons in the bilayer MoS<sub>2</sub>. (g) *Ab initio* calculated changes of the high-symmetry points *K* and *K'* and *Q* and *Q'* as a function of an external applied electric field *F* for the top and bottom layers.

and

$$\dot{n}_Q = (1 - c)n_0 - \frac{n_Q}{T_Q}, \quad (2)$$

where  $n_X$  is the electronic population in the *X* state and  $\dot{n}_X$  its time derivative.  $\tau_K$  is the radiative recombination lifetime and  $T_K$  and  $T_Q$  are the lifetime for nonradiative recombination channels in each valley, *K* and *Q*, respectively.

The application of a gate voltage generates additional transitions that modify the steady state and consequently the polarization of the photoluminescence. These transitions are labeled as (i) and (ii) in Fig. 3(e) for the *Q* to *K* scattering case. The green arrows represent the polarization of the *Q* valley that facilitates the transfer of electrons to the bottom layer. This is the central effect in this model affecting the

circular polarization degree for all multilayer samples. The redistribution of electrons via the *Q* point manifests in the formation of intra- and interlayer excitons in the bilayer [see Fig 3(f)]. The field-dependent first-principles calculations and corresponding energy shifts of the *K* and *Q* points in Fig. 3(g) show, as the most important effect, a strong reduction of the energy distance between the  $K_2^\uparrow$  point and the *Q* valley. This enhances transition (ii) at the same time that transition (i) appears to have, in comparison, a reduced contribution. On the other hand, the outstanding effect of the gate voltage is the population increase of electrons in bright states (*K* point) at the expense of dark states (*Q* valley) and this effect can be well described by subtracting  $A(V)n_Q/T_{QK}$  from the *Q* valley rate equation. Here,  $A(V)$  accounts for the tunability of the system with gate voltage *V*, and  $T_{QK}$  represents the lifetime

for transition (ii). This term constitutes a source term for the latter level, whose complete rate equation is

$$\dot{n}_{K_2^\uparrow} = A(V) \frac{n_Q}{T_{QK}} - \frac{n_{K_2^\uparrow}}{\tau_{K'}} - \frac{n_{K_2^\uparrow}}{T_K}. \quad (3)$$

We model the function  $A(V)$  as an exponential growth (see Supplemental Material [33] for details),

$$A = e^{\frac{V-V_0}{V_0}} - e^{-1}, \quad (4)$$

whose value is identically zero for  $V = 0$  V and  $V_0$  is a fitting parameter. It is important to note that the interlayer exciton in MoS<sub>2</sub> is the result of a strong admixture between a  $B$  intralayer exciton and an  $A$  interlayer exciton [19,21,22,52]. While resonant excitation at 1.96 eV can create finite interlayer exciton PL, we only calculate the degree of valley polarization for energies well below such energies to only take into account changes in the  $A$ -exciton polarized emission. Moreover, holes are strongly localized in the top layer and the recombination process from the  $K_2^\uparrow$  level would describe the annihilation of *interlayer* excitons with radiative and non-radiative lifetimes of  $\tau_{K'}$  and  $T_{K'}$ , respectively. In the case of scattering from  $Q'$  and  $K'$ , the excitation with  $\sigma^+$  light generates spin-up electrons in  $Q'$  of the bilayer and  $K_2^\uparrow$  of the bottom layer with similar dynamics as in the  $Q$  and  $K$  points. Including the gate-voltage effect which activates the transition labeled (iii) in Fig. 3(e), their rate equations are

$$\dot{n}_{K_2^\uparrow} = cn_0 - \frac{n_{K_2^\uparrow}}{\tau_K} - \frac{n_{K_2^\uparrow}}{T_K} + A(V) \frac{n_Q}{T_{QK}} \quad (5)$$

and

$$\dot{n}_{Q'} = (1 - c)n_0 - \frac{n_{Q'}}{T_Q} - A(V) \frac{n_{Q'}}{T_{QK}}. \quad (6)$$

Since both layers are equivalent, the radiative and non-radiative lifetimes involved in the process are the same. In addition,  $Q$  and  $Q'$  are also equivalent points of the bilayer with the same nonradiative lifetime.

All the radiative transitions described in the rate equations above correspond to light emitted with  $\sigma^+$  polarization. By solving these equations in the steady state with realistic material parameters, we determine the  $\sigma^+$ -polarized emission intensity as a function of  $V$  and calculate the circular polarization degree of the PL using  $c$ ,  $s$ , and  $V_0$  as fitting parameters. Note that this emission originates from both intra- and interlayer excitons [see Fig. 3(f)]. The total  $\sigma^+$  emission is then the sum of both processes. The calculated electric-field-dependent circular polarization degree is presented in Fig. 3(a), showing excellent agreement with the experiment. Both data sets are fitted individually due to a small difference in the voltage offset that originates from the subsequent recording of data and the hysteresis of the device [29]. The corresponding material and fitting parameters are listed in the Supplemental Material [33].

Since our model stems from steady-state electron distributions, similar dependencies of  $\eta$  are expected for systems with more than two layers. Indeed, probing the trilayer MoS<sub>2</sub>, we obtain a similar modulation of  $\eta$  as shown in Fig. 4(a). For the case where the symmetry between the layers is restored ( $-60$  V), we obtain a minimum  $\eta \sim 0.15$ , while for the highest electric field ( $-120$  V), a maximum  $\eta \sim 0.35$  is observed.

Similar to the bilayer case, we find a strong delocalization of the electron wave function at the  $Q$  points [see Figs. 4(b) and 4(c)], suggesting a similar steady-state population redistribution of electrons throughout the trilayer. The level scheme for a trilayer is analogous to the bilayer by adding an additional layer as shown in Fig. 4(d) for an applied electric field. Similar to the bilayer, it allows the formation of intra- and interlayer excitons [see Fig. 4(e)]. The computed CB and valence band (VB) edges of  $K$  and  $K'$  and  $Q$  and  $Q'$  points are shown in Fig. 4(f). For a finite field of  $>2 \times 10^{-4}$  V Å<sup>-1</sup>, the energy sequence in the CB and VB follows the stacking order of the layers, resulting in a field-dependent electron distribution throughout the trilayer that is mediated via the  $Q$  point [see Fig. 4(d)]. We solved the rate-equation model for a trilayer system [see Fig. 4(d)] analogously to the bilayer. The resulting  $\eta$  is again in excellent agreement with experimental data [see Fig. 4(a)].

The valley optical selection rules in TMDCs are strongly connected to the crystal inversion symmetry and time-reversal symmetry (Kramers degeneracy). 2H trilayer TMDCs are intrinsically inversion symmetry broken and, therefore, tunability of the optical valley dichroism is not expected. This results for example in a nontunable second-harmonic generation [7]. However, our observation of field-tunable  $\eta$  in the trilayer suggests that the breaking of the Kramers degeneracy and the accompanying occurrence of a valley magnetic moment [4] is not sufficient to explain our data [see Fig. 4(a)]. Our results and microscopic modeling based on DFT calculation input suggest that the high-symmetry  $Q$  point and a field-dependent change in the *interlayer* hybridization, and therefore *interlayer* hopping, can strongly modify the steady-state electron and, therefore, exciton population in the bi- and trilayer system manifesting in the tunable valley dichroism. This is in contrast to earlier work that attributed it solely to a change in the valley magnetic moment [4,15]. Moreover, our field-dependent DFT calculations of electron and hole populations in the conduction band at the  $Q$  point and in the valence band at the  $\Gamma$  point show that the dominant mechanism of charge transfer is indeed dominated by the  $Q$  point (see the Supplemental Material [33]).

### III. CONCLUSION

In summary, we demonstrated the electrical control of interlayer vibrational and orbital coupling in bi- and trilayer MoS<sub>2</sub>. Field-dependent Raman spectroscopy is a useful tool to probe the symmetry and layer decoupling of bi- and trilayer crystals. Our work suggests that the  $Q$  point in multilayer TMDCs is important for understanding steady-state electron populations and, therefore, the spin-valley dichroism of TMDCs and other vdW heterostructures.

### ACKNOWLEDGMENTS

We gratefully acknowledge financial support from the ExQM Ph.D. program of the sElite Network of Bavaria, the German Excellence Initiative via the Nanosystems Initiative Munich (NIM), the Deutsche Forschungsgemeinschaft (DFG) via the clusters of excellence e-conversion (EXC 2111) and MCQST (EXC 2089), via SPP 2244, the European Union's

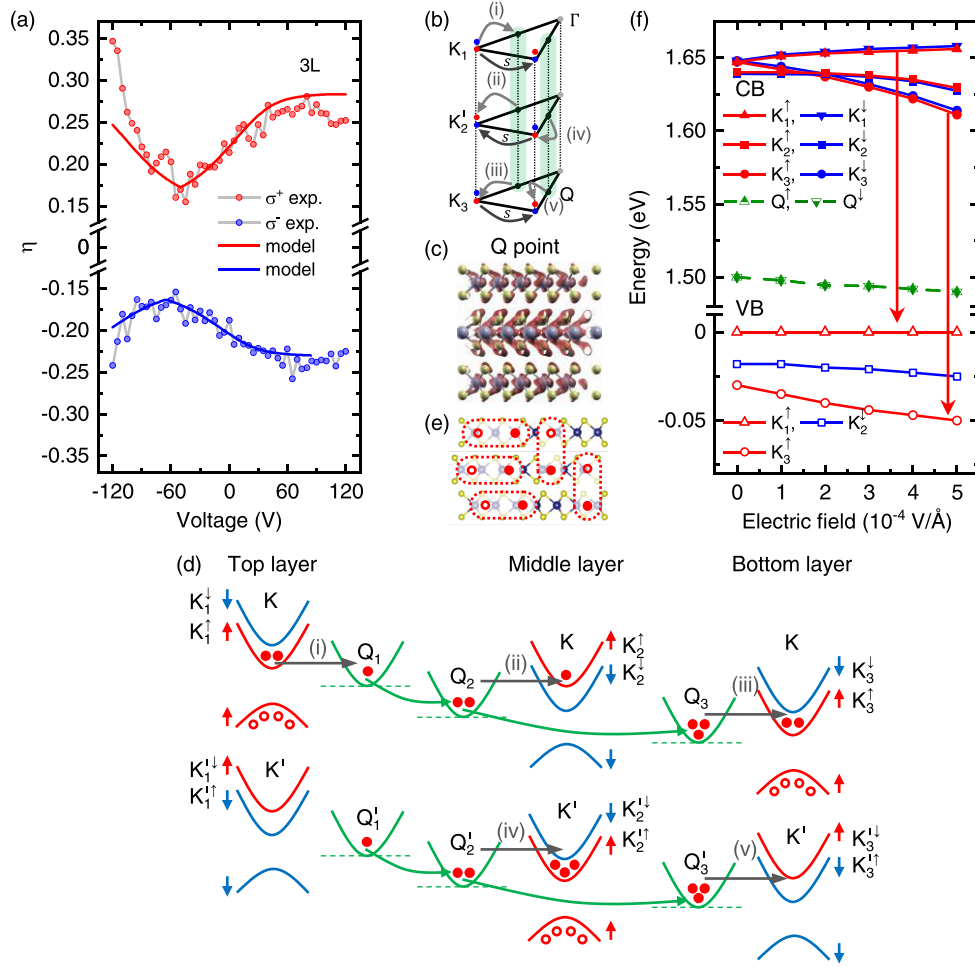


FIG. 4. (a) Tuning of orbital interlayer coupling in trilayer MoS<sub>2</sub>. Voltage-controlled degree of valley polarization for  $\sigma^+$  (red circles) and  $\sigma^-$  (blue circles) excitation. The solid lines are the calculated rate-equation model. (b) First Brillouin zone and high-symmetry points of the trilayer MoS<sub>2</sub>. The scattering pathways (i)–(v) of electrons are highlighted in addition to *intralayer* and *intervalley* scattering *s*. (c) *Ab initio* calculated wave-function distribution at the *Q* point is strongly delocalized between top, middle, and bottom layers. (d) Schematic of the rate-equation model used for describing the voltage-controlled  $\eta$  for an applied external electric field. (e) The trilayer hosts intra- and interlayer excitons. (f) *Ab initio* calculated changes of the high-symmetry points *K* and *K'* and *Q* as a function of an external applied electric field *F* for the top, middle, and bottom layers.

Horizon 2020 research and innovation programme under Grant Agreement No. 820423 (S2QUIP) and through the TUM International Graduate School of Science and Engineering (IGSSE). J.K. acknowledges support by the Alexander von Humboldt foundation. A.K. acknowledges DFG project GRK 2247/1 (QM3), and the association with SPP 2244. A.K. and T.B. acknowledge the support by the DFT within SFB 1415, No. 417590517 and the high-performance computing center of ZIH Dresden for computational resources. We further thank Ursula Wurstbauer and Andor Kormányos for insightful and stimulating discussions.

J.K., J.W., K.M., and J.J.F. conceived and designed the experiments, J.K. and J.W. prepared the samples, J.K. and J.W. performed the optical measurements, J.K. analyzed the data, P.S., J.K. and A.V.S. developed the rate equation model, A.K. and L.M. computed the electric-field-dependent Raman and phonon-dispersion spectra, T.B. computed the field-dependent electronic band structures, and J.K. wrote the paper with input from all co-authors. All authors reviewed the manuscript.

The authors declare no competing financial interest.

## APPENDIX: METHODS

### 1. Device fabrication

The MoS<sub>2</sub> crystal is mechanically exfoliated onto a 295-nm-thick SiO<sub>2</sub> layer on a heavily *n*-doped silicon substrate. Spatially resolved Raman spectroscopy and white light interferometry are used to identify mono-, bi-, and trilayer regions of the flake, before it is capped with a 20-nm-thick Al<sub>2</sub>O<sub>3</sub> dielectric using atomic layer deposition (ALD) at a low temperature of 120 °C. An electrical contact is established to the silicon substrate and the sample is completed with a 5-nm-thick semitransparent titanium top contact that facilitates optical access to the crystal while tuning the gate voltage (electric field) in the range  $\pm 120$  V. The device fabrication procedure is found to have no significant deleterious impact on the photoluminescence properties of the atomically thin flake. Further details of the fabrication, electrical characterization, and control of the *A*-exciton emission energies using

the dc Stark effect and control of second-harmonic generation (SHG) can be found in Refs. [29] and [7].

## 2. Optical spectroscopy

For low-temperature confocal microphotoluminescence ( $\mu$ -PL) and Raman measurements we keep the device under vacuum in a helium flow cryostat with a lattice temperature kept at  $T = 10$  K. For circularly polarized measurements, we use a HeNe laser with an excitation energy of 1.96 eV. An excitation power density of  $\sim 10$  kW cm $^{-2}$  is used. The laser spot has a diameter of  $d_{\text{spot}} \sim 1.2$   $\mu$ m.

## 3. DFT calculations

All materials (1L-3L MoS $_2$ ) were fully optimized, including the lattice parameters and the atomic positions using density-functional theory with Perdew-Burke-Ernzerhof (PBE) [61] exchange-correlation functional together with D3 London dispersion correction [62] as implemented in CRYSTAL17 [63,64]. The resulting lattice parameters  $a$  and  $b$  are 3.137 Å for 1L, 3.136 Å for 2L, and 3.135 Å for 3L, while interlayer distance between metal centers is  $d = 5.956$  Å. For Mo atoms, we used a small-core effective-core pseudopotential (ECP) of Hay-Wadt type [65] which accounted for the

electrons  $1s^2-3d^{10}$ , while for S atoms, we used 86 – 311G\* [66]. The  $8 \times 8 \times 1$   $k$ -point grid was used for structural relaxation. For Raman and phonon-dispersion calculations, geometries were reoptimized, applying external electric field of a given strength perpendicular to the basal plane of the layers. Phonon-dispersion calculations were performed using a finite displacement method on the  $5 \times 5 \times 1$  supercells. Raman active modes were calculated at the  $\Gamma$  point.

Using the geometries as relaxed with CRYSTAL17, the field-dependent electronic band structures and the corresponding spin projections have been calculated within the framework of DFT as implemented in the QUANTUM ESPRESSO package [67,68]. We employed full-relativistic, projector-augmented wave potentials [69] of the version 1.0.0 of the pslibrary [70] and we also chose the PBE [61] for the exchange-correlation energy. Cutoffs of 60 and 480 Ry (1 Ry  $\approx$  13.6 eV) for the wave functions and the charge density, respectively, were used. The convergence was checked with higher cutoffs which led to only slight shifts of the semicore states at energies lower than  $\approx -30$  eV below the Fermi energy. The Brillouin zone integration was performed with a  $\Gamma$ -centered Monkhorst-Pack grid [71] of  $18 \times 18 \times 1$   $k$ -points together with a Gaussian broadening of 0.005 Ry. The self-consistent solution of the Kohn-Sham equations was obtained when the total energy changed by less than  $10^{-10}$  Ry.

- 
- [1] Y. Zhang, T.-T. Tang, C. Girit, Z. Hao, M. C. Martin, A. Zettl, M. F. Crommie, Y. R. Shen, and F. Wang, *Nature (London)* **459**, 820 (2009).
- [2] M. Sui, G. Chen, L. Ma, W.-Y. Shan, D. Tian, K. Watanabe, T. Taniguchi, X. Jin, W. Yao, D. Xiao, and Y. Zhang, *Nat. Phys.* **11**, 1027 (2015).
- [3] Y. Shimazaki, M. Yamamoto, I. V. Borzenets, K. Watanabe, T. Taniguchi, and S. Tarucha, *Nat. Phys.* **11**, 1032 (2015).
- [4] S. Wu, J. S. Ross, G.-B. Liu, G. Aivazian, A. Jones, Z. Fei, W. Zhu, D. Xiao, W. Yao, D. Cobden, and X. Xu, *Nat. Phys.* **9**, 149 (2013).
- [5] A. M. Jones, H. Yu, J. S. Ross, P. Klement, N. J. Ghimire, J. Yan, D. G. Mandrus, W. Yao, and X. Xu, *Nat. Phys.* **10**, 130 (2014).
- [6] J. Lee, K. F. Mak, and J. Shan, *Nat. Nanotechnol.* **11**, 421 (2016).
- [7] J. Klein, J. Wierzbowski, A. Steinhoff, M. Florian, M. Rösner, F. Heimbach, K. Müller, F. Jahnke, T. O. Wehling, J. J. Finley, and M. Kaniber, *Nano Lett.* **17**, 392 (2017).
- [8] L. Du, T. Hasan, A. Castellanos-Gomez, G.-B. Liu, Y. Yao, C. N. Lau, and Z. Sun, *Nat. Rev. Phys.* **3**, 193 (2021).
- [9] K. F. Mak, C. Lee, J. Hone, J. Shan, and T. F. Heinz, *Phys. Rev. Lett.* **105**, 136805 (2010).
- [10] A. Splendiani, L. Sun, Y. Zhang, T. Li, J. Kim, C.-Y. Chim, G. Galli, and F. Wang, *Nano Lett.* **10**, 1271 (2010).
- [11] K. F. Mak, K. He, J. Shan, and T. F. Heinz, *Nat. Nanotechnol.* **7**, 494 (2012).
- [12] H. Zeng, J. Dai, W. Yao, D. Xiao, and X. Cui, *Nat. Nanotechnol.* **7**, 490 (2012).
- [13] T. Cao, G. Wang, W. Han, H. Ye, C. Zhu, J. Shi, Q. Niu, P. Tan, E. Wang, B. Liu, and J. Feng, *Nat. Commun.* **3**, 887 (2012).
- [14] G. Sallen, L. Bouet, X. Marie, G. Wang, C. R. Zhu, W. P. Han, Y. Lu, P. H. Tan, T. Amand, B. L. Liu, and B. Urbaszek, *Phys. Rev. B* **86**, 081301(R) (2012).
- [15] A. Kormányos, V. Zólyomi, V. I. Falko, and G. Burkard, *Phys. Rev. B* **98**, 035408 (2018).
- [16] B. Miller, A. Steinhoff, B. Pano, J. Klein, F. Jahnke, A. Holleitner, and U. Wurstbauer, *Nano Lett.* **17**, 5229 (2017).
- [17] Y. Wang, Z. Wang, W. Yao, G.-B. Liu, and H. Yu, *Phys. Rev. B* **95**, 115429 (2017).
- [18] C. Jin, E. Y. Ma, O. Karni, E. C. Regan, F. Wang, and T. F. Heinz, *Nat. Nanotechnol.* **13**, 994 (2018).
- [19] I. C. Gerber, E. Courtade, S. Shree, C. Robert, T. Taniguchi, K. Watanabe, A. Balocchi, P. Renucci, D. Lagarde, X. Marie, and B. Urbaszek, *Phys. Rev. B* **99**, 035443 (2019).
- [20] I. Paradisanos, S. Shree, A. George, N. Leisgang, C. Robert, K. Watanabe, T. Taniguchi, R. J. Warburton, A. Turchanin, X. Marie, I. C. Gerber, and B. Urbaszek, *Nat. Commun.* **11**, 2391 (2020).
- [21] N. Leisgang, S. Shree, I. Paradisanos, L. Sponfeldner, C. Robert, D. Lagarde, A. Balocchi, K. Watanabe, T. Taniguchi, X. Marie, R. J. Warburton, I. C. Gerber, and B. Urbaszek, *Nat. Nanotechnol.* **15**, 901 (2020).
- [22] N. Peimyoo, T. Deilmann, F. Withers, J. Escobar, D. Nutting, T. Taniguchi, K. Watanabe, A. Taghizadeh, M. F. Craciun, K. S. Thygesen, and S. Russo, *Nat. Nanotechnol.* **16**, 888 (2021).
- [23] E. Lorchat, M. Selig, F. Katsch, K. Yumigeta, S. Tongay, A. Knorr, C. Schneider, and S. Höfling, *Phys. Rev. Lett.* **126**, 037401 (2021).
- [24] Y. Zhao, L. Du, S. Yang, J. Tian, X. Li, C. Shen, J. Tang, Y. Chu, K. Watanabe, T. Taniguchi, R. Yang, D. Shi, Z. Sun, Y. Ye, W. Yang, and G. Zhang, *arXiv:2106.00351*.

- [25] X. Hong, J. Kim, S.-F. Shi, Y. Zhang, C. Jin, Y. Sun, S. Tongay, J. Wu, Y. Zhang, and F. Wang, *Nat. Nanotechnol.* **9**, 682 (2014).
- [26] J. Kiemle, F. Sigger, M. Lorke, B. Müller, K. Watanabe, T. Taniguchi, A. Holleitner, and U. Wurstbauer, *Phys. Rev. B* **101**, 121404(R) (2020).
- [27] S. Gao, L. Yang, and C. D. Spataru, *Nano Lett.* **17**, 7809 (2017).
- [28] Y. Shimazaki, I. Schwartz, K. Watanabe, T. Taniguchi, M. Kroner, and A. Imamoğlu, *Nature (London)* **580**, 472 (2020).
- [29] J. Klein, J. Wierzbowski, A. Regler, J. Becker, F. Heimbach, K. Müller, M. Kaniber, and J. J. Finley, *Nano Lett.* **16**, 1554 (2016).
- [30] J. L. Verble and T. J. Wieting, *Phys. Rev. Lett.* **25**, 362 (1970).
- [31] A. Molina-Sánchez and L. Wirtz, *Phys. Rev. B* **84**, 155413 (2011).
- [32] Y. Zhao, X. Luo, H. Li, J. Zhang, P. T. Araujo, C. K. Gan, J. Wu, H. Zhang, S. Y. Quek, M. S. Dresselhaus, and Q. Xiong, *Nano Lett.* **13**, 1007 (2013).
- [33] See Supplemental Material at <http://link.aps.org/supplemental/10.1103/PhysRevMaterials.6.024002> for experimental setup to probe the circular polarization, gate-voltage-dependent Raman spectra of bi- and trilayer MoS<sub>2</sub>, DFT-calculated phonon dispersion with external electric field, degree of circular polarization on SiO<sub>2</sub>/Si, degree of circular polarization in the microapacitor, DFT-calculated electronic band structure with external electric field, DFT-calculated wave functions of valence and conduction bands in bi- and trilayer MoS<sub>2</sub>, DFT-calculated wave-function contribution of electrons and holes at high-symmetry points for bi- and trilayer MoS<sub>2</sub>, as well as details on the rate-equation model.
- [34] B. Müller, J. Lindlau, M. Bommert, A. Neumann, H. Yamaguchi, A. Holleitner, A. Högele, and U. Wurstbauer, *Nat. Commun.* **10**, 807 (2019).
- [35] B. Chakraborty, A. Bera, D. V. S. Muthu, S. Bhowmick, U. V. Waghmare, and A. K. Sood, *Phys. Rev. B* **85**, 161403(R) (2012).
- [36] M. Staiger, R. Gillen, N. Scheuschner, O. Ochedowski, F. Kampmann, M. Schleberger, C. Thomsen, and J. Maultzsch, *Phys. Rev. B* **91**, 195419 (2015).
- [37] L. Du, Z. Jia, Q. Zhang, A. Zhang, T. Zhang, R. He, R. Yang, D. Shi, Y. Yao, J. Xiang, G. Zhang, and Q. Zhang, *2D Mater.* **5**, 035028 (2018).
- [38] M. Palumbo, M. Bernardi, and J. C. Grossman, *Nano Lett.* **15**, 2794 (2015).
- [39] C. Robert, D. Lagarde, F. Cadiz, G. Wang, B. Lassagne, T. Amand, A. Balocchi, P. Renucci, S. Tongay, B. Urbaszek, and X. Marie, *Phys. Rev. B* **93**, 205423 (2016).
- [40] G. Kioseoglou, A. T. Hanbicki, M. Currie, A. L. Friedman, D. Gunlycke, and B. T. Jonker, *Appl. Phys. Lett.* **101**, 221907 (2012).
- [41] B. Zhu, H. Zeng, J. Dai, Z. Gong, and X. Cui, *Proc. Natl. Acad. Sci. USA* **111**, 11606 (2014).
- [42] R. Suzuki, M. Sakano, Y. J. Zhang, R. Akashi, D. Morikawa, A. Harasawa, K. Yaji, K. Kuroda, K. Miyamoto, T. Okuda, K. Ishizaka, R. Arita, and Y. Iwasa, *Nat. Nanotechnol.* **9**, 611 (2014).
- [43] X. Zhang, J. Zhou, S.-Q. Li, Y. Wang, S. Zhang, Y. Liu, J. Gao, J. Zhao, W. Wang, R. Yu, W. Zhang, N. Liu, J. Nie, L. He, and R. Dou, *J. Phys. Chem. Lett.* **12**, 5879 (2021).
- [44] C. Robert, B. Han, P. Kapuscinski, A. Delhomme, C. Faugeras, T. Amand, M. R. Molas, M. Bartos, K. Watanabe, T. Taniguchi, B. Urbaszek, M. Potemski, and X. Marie, *Nat. Commun.* **11**, 4037 (2020).
- [45] J. Klein, A. Hötger, M. Florian, A. Steinhoff, A. Delhomme, T. Taniguchi, K. Watanabe, F. Jahnke, A. W. Holleitner, M. Potemski, C. Faugeras, J. J. Finley, and A. V. Stier, *Phys. Rev. Research* **3**, L022009 (2021).
- [46] J. Klein, M. Florian, A. Hötger, A. Steinhoff, A. Delhomme, T. Taniguchi, K. Watanabe, F. Jahnke, A. W. Holleitner, M. Potemski, C. Faugeras, A. V. Stier, and J. J. Finley, *Phys. Rev. B* **105**, L041302 (2022).
- [47] Q. Liu, X. Zhang, and A. Zunger, *Phys. Rev. Lett.* **114**, 087402 (2015).
- [48] L. Yuan, Q. Liu, X. Zhang, J.-W. Luo, S.-S. Li, and A. Zunger, *Nat. Commun.* **10**, 906 (2019).
- [49] L. Du, M. Liao, G.-B. Liu, Q. Wang, R. Yang, D. Shi, Y. Yao, and G. Zhang, *Phys. Rev. B* **99**, 195415 (2019).
- [50] G.-B. Liu, W.-Y. Shan, Y. Yao, W. Yao, and D. Xiao, *Phys. Rev. B* **88**, 085433 (2013).
- [51] Z. Gong, G.-B. Liu, H. Yu, D. Xiao, X. Cui, X. Xu, and W. Yao, *Nat. Commun.* **4**, 2053 (2013).
- [52] T. Deilmann and K. S. Thygesen, *Nano Lett.* **18**, 2984 (2018).
- [53] A. O. Slobodeniuk, Ł. Bala, M. Koperski, M. R. Molas, P. Kossacki, K. Nogajewski, M. Bartos, K. Watanabe, T. Taniguchi, C. Faugeras, and M. Potemski, *2D Mater.* **6**, 025026 (2019).
- [54] L. Guo, M. Wu, T. Cao, D. M. Monahan, Y.-H. Lee, S. G. Louie, and G. R. Fleming, *Nat. Phys.* **15**, 228 (2019).
- [55] W.-T. Hsu, B.-H. Lin, L.-S. Lu, M.-H. Lee, M.-W. Chu, L.-J. Li, W. Yao, W.-H. Chang, and C.-K. Shih, *Sci. Adv.* **5**, eaax7407 (2019).
- [56] A. Steinhoff, M. Rösner, F. Jahnke, T. O. Wehling, and C. Gies, *Nano Lett.* **14**, 3743 (2014).
- [57] A. Steinhoff, J.-H. Kim, F. Jahnke, M. Rösner, D.-S. Kim, C. Lee, G. H. Han, M. S. Jeong, T. O. Wehling, and C. Gies, *Nano Lett.* **15**, 6841 (2015).
- [58] A. Steinhoff, M. Florian, M. Rösner, M. Lorke, T. O. Wehling, C. Gies, and F. Jahnke, *2D Mater.* **3**, 031006 (2016).
- [59] R. Wallauer, J. Reimann, N. Armbrust, J. Gütde, and U. Höfer, *Appl. Phys. Lett.* **109**, 162102 (2016).
- [60] J. Madéo, M. K. L. Man, C. Sahoo, M. Campbell, V. Pareek, E. L. Wong, A. Al-Mahboob, N. S. Chan, A. Karmakar, B. M. K. Mariserla, X. Li, T. F. Heinz, T. Cao, and K. M. Dani, *Science* **370**, 1199 (2020).
- [61] J. P. Perdew, K. Burke, and M. Ernzerhof, *Phys. Rev. Lett.* **77**, 3865 (1996).
- [62] S. Grimme, *J. Comput. Chem.* **27**, 1787 (2006).
- [63] R. Dovesi, V. R. Saunders, C. Roetti, R. Orlando, C. M. Zicovich-Wilson, F. Pascale, B. Civalleri, K. Doll, N. M. Harrison, I. J. Bush, P. D'Arco, M. Llunell, M. Causá, Y. Noël, L. Maschio, A. Erba, M. Rerat, and S. Casassa, *CRYSTAL17 User's Manual* (University of Torino, Torino, 2017).
- [64] R. Dovesi, A. Erba, R. Orlando, C. M. Zicovich-Wilson, B. Civalleri, L. Maschio, M. Rérat, S. Casassa, J. Baima, S. Salustro, and B. Kirtman, *WIREs Comput. Mol. Sci.* **8**, 1360 (2018).
- [65] F. Corà, A. Patel, N. M. Harrison, C. Roetti, and C. R. A. Catlow, *J. Mater. Chem.* **7**, 959 (1997).
- [66] A. Lichanot, E. Aprà, and R. Dovesi, *Phys. Status Solidi B* **177**, 157 (1993).

- [67] P. Giannozzi, S. Baroni, N. Bonini, M. Calandra, R. Car, C. Cavazzoni, D. Ceresoli, G. L. Chiarotti, M. Cococcioni, I. Dabo, A. D. Corso, S. de Gironcoli, S. Fabris, G. Fratesi, R. Gebauer, U. Gerstmann, C. Gougoussis, A. Kokalj, M. Lazzeri, L. Martin-Samos, N. Marzari, F. Mauri, R. Mazzarello, S. Paolini, A. Pasquarello, L. Paulatto, C. Sbraccia, S. Scandolo, G. Sclauzero, A. P. Seitsonen, A. Smogunov, P. Umari, and R. M. Wentzcovitch, *J. Phys.: Condens. Matter* **21**, 395502 (2009).
- [68] P. Giannozzi, Jr., O. Andreussi, T. Brumme, O. Bunau, M. B. Nardelli, M. Calandra, R. Car, C. Cavazzoni, D. Ceresoli, M. Cococcioni, N. Colonna, I. Carnimeo, A. D. Corso, S. de Gironcoli, P. Delugas, R. A. DiStasio, A. Ferretti, A. Floris, G. Fratesi, G. Fugallo, R. Gebauer, U. Gerstmann, F. Giustino, T. Gorni, J. Jia, M. Kawamura, H.-Y. Ko, A. Kokalj, E. Küçükbenli, M. Lazzeri, M. Marsili, N. Marzari, F. Mauri, N. L. Nguyen, H.-V. Nguyen, A. O. de-la Roza, L. Paulatto, S. Poncé, D. Rocca, R. Sabatini, B. Santra, M. Schlipf, A. P. Seitsonen, A. Smogunov, I. Timrov, T. Thonhauser, P. Umari, N. Vast, X. Wu, and S. Baroni, *J. Phys.: Condens. Matter* **29**, 465901 (2017).
- [69] G. Kresse and D. Joubert, *Phys. Rev. B* **59**, 1758 (1999).
- [70] A. D. Corso, *Comput. Mater. Sci.* **95**, 337 (2014); See <https://dalcorso.github.io/pslibrary/> for more details.
- [71] H. J. Monkhorst and J. D. Pack, *Phys. Rev. B* **13**, 5188 (1976).